symmetry

MDPI

Article

Determining Ground-State Phase Diagrams on Quantum Computers via a Generalized Application of Adiabatic State Preparation

Akhil Francis [1], Ephrata Zelleke [2], Ziyue Zhang [3], Alexander F. Kemper [1,*] and James K. Freericks [3]

[1] Department of Physics, North Carolina State University, Raleigh, NC 27695, USA; afranci2@ncsu.edu
[2] Department of Physics, Goucher College, Baltimore, MD 21204, USA; ezellek1@jhu.edu
[3] Department of Physics, Georgetown University, Washington, DC 20057, USA; zz166@georgetown.edu (Z.Z.); james.freericks@georgetown.edu (J.K.F.)
* Correspondence: akemper@ncsu.edu; Tel.: +1-919-515-7339

Abstract: Quantum phase transitions materialize as level crossings in the ground-state energy when the parameters of the Hamiltonian are varied. The resulting ground-state phase diagrams are straightforward to determine by exact diagonalization on classical computers, but are challenging on quantum computers because of the accuracy needed and the near degeneracy of the competing states close to the level crossings. On the other hand, classical computers are limited to small system sizes, which quantum computers may help overcome. In this work, we use a local adiabatic ramp for state preparation to allow us to directly compute ground-state phase diagrams on a quantum computer via time evolution. This methodology is illustrated by examining the ground states of the XY model with a magnetic field in the z-direction in one dimension. We are able to calculate an accurate phase diagram on both two- and three-site systems using IBM quantum machines.

Keywords: quantum phase transition; adiabatic evolution; quantum computing; XY model; superconducting qubits

Citation: Francis, A.; Zelleke, E.; Zhang, Z.; Kemper, A.F.; Freericks, J.K. Determining Ground-State Phase Diagrams on Quantum Computers via a Generalized Application of Adiabatic State Preparation. *Symmetry* **2022**, *14*, 809. https://doi.org/10.3390/sym14040809

Academic Editor: Tomohiro Inagaki

Received: 22 February 2022
Accepted: 8 April 2022
Published: 13 April 2022

1. Introduction

Quantum computers are thought to enable calculations that cannot be carried out on classical computers [1–5]. For simulating quantum systems, classical computers are limited to exact diagonalization as there are no good approximation methods available in general. However, exact diagonalization cannot be employed in large systems, as the Hilbert space grows exponentially with respect to the system size [3]. One challenging problem in many-body physics is to determine the zero-temperature phase diagram of finite systems that have level crossings in the ground state as the parameters in the Hamiltonian are tuned across the transition [6,7]. Such phase diagrams commonly occur when a system has competing order parameters [8]. One possible approach to solving this problem is to simply create circuits for target wave functions that can have their parameters varied to allow for a variational determination of the approximate ground state. Then, one can determine the phase diagram by examining the quantum numbers and the symmetries of the variational wave function. However, such an approach is likely to fail or to be inaccurate; this is because there are low-lying states near the level crossings and the variational calculations need to be done with high accuracy to carry out such a program. This becomes especially complicated if the variational state ansatz does not belong to the subspace corresponding to the ground-state quantum numbers.

Another approach one could try is to use adiabatic state preparation: start the system in an easy to prepare state that is the ground state of the Hamiltonian for a given parameter, and then slowly change the parameters in the Hamiltonian. If we change slowly enough, the adiabatic theorem guarantees that we stay in the ground state. This approach may

also have problems, because the time evolution will preserve the symmetry of the wave function, and level crossings can only occur between states with different symmetries.

However, we can modify the adiabatic state preparation protocol by adding a small symmetry-breaking field, and we can find the phase transition point by monitoring the expectation value of the quantum numbers corresponding to the different symmetries on either side of the phase transition. Now, because the symmetries are only approximate, a sufficiently slow time evolution will map out the ground-state phase diagram. We then repeat with different magnitudes of the symmetry-breaking field and extrapolate the results to the limit where the symmetry-breaking field vanishes. In this fashion, we can employ adiabatic state preparation to carry out a mapping of the ground-state phase diagram. It is unlikely that fast forwarding techniques such as QAOA [9] or shortcuts to adiabaticity [10,11], will help with carrying out this approach because it may require very accurate optimization near the level crossing, or knowledge of the eigenstates or invariants of motion, which maybe costly to find.

We test our approach on the ground-state phase diagram of an isotropic 1D XY model in a magnetic field along the z-direction. This system is a stringent test for such an approach, because there are N phase transitions for an N-site system in the region where $|B_z| \leq |J|$. As the system size is made larger, the problem becomes increasingly more challenging to solve. In fact, the model may exhibit a devil's staircase in the ground-state phase diagram [12]. The conserved symmetry (quantum number) is the z-component of total spin, so we can monitor the phase diagram by measuring the magnetization of the system.

Our strategy is to start the system in a large B_z field, and to add a small symmetry-breaking field B_x in a perpendicular direction. The initial state will be taken to be polarized along the z-direction, which is easy to prepare. We ramp the z-field down, keeping the x-field fixed, using a local adiabatic ramp [13]. This approach was originally used to generate the ground state of the transverse-field Ising model in ion-trap quantum simulators. For the two-site system, we also performed the experiment starting from all spins aligned down and ramping up the B_z field. We find that for two- and three-site systems, this approach gives accurate phase diagrams in IBM quantum machines.

2. Materials and Methods

We work with the one-dimensional isotropic XY model with periodic boundary conditions and a magnetic field along the z direction, as shown in Equation (1) for a system with L spins:

$$H = -\sum_{i=1}^{L}\left[\frac{J}{4}\left(\sigma_i^x\sigma_{i+1}^x + \sigma_i^y\sigma_{i+1}^y\right) + \frac{B_z}{2}\sigma_i^z\right]. \tag{1}$$

where $\sigma_i^{x,y,z}$ are the usual Pauli matrices obtained by setting ($\hbar = 1$) in the spin operators of the ith site, $S_i^{x,y,z} = \frac{\hbar}{2}\sigma_i^{x,y,z}$. This model can be solved exactly by fermionization using a Jordan–Wigner (JW) transformation [14] and a subsequent Fourier transformation to momentum space [15]. The boundary term needs more care as it still has the JW string in it. Usually, for a large system this term is negligible. Alternatively, we simply consider the periodic term without a JW string attached, so that the usual Fourier transform yields the fermionic eigen energies. Then, the fermionic Hamiltonian takes the form

$$H = \sum_k\left(\omega_k c_k^\dagger c_k - \frac{B_z}{2}\right) \tag{2}$$

where $\omega_k = (-J\cos k + B_z)$ and $k = \frac{2n\pi}{L}$, with $n = -\frac{L}{2}+1, \cdots, 0, \cdots, \frac{L}{2}$.

For a finite-size system the boundary term matters; this can be dealt with by making use of the fermionic parity [16]. The system is decoupled into odd and even parity sectors, where periodic and anti-periodic boundary terms emerge, respectively. This results in the same form for the fermionic Hamiltonian, but with different momenta for the different parity sectors. For odd parity sector, the momenta are the ones mentioned above (which

includes the zero momentum point), whereas for an even parity sector, the momenta are shifted to $k = \pm\frac{(2n-1)\pi}{L}$, with $n = 1, \cdots, \frac{L}{2}$. One challenge with this approach is that each parity sector has 2^L eigenvalues while the exact solution (over both parities) has exactly 2^L eigenvalues. To avoid any of these issues, we work in the original spin representation throughout this paper.

The ground state has many level crossings as a function of the magnetic field B_z. This is illustrated in Figures 1 and 2. Figure 1 shows the expectation value of the z-component of spin (also known as the magnetization) as a function of B_z. Each of the vertical steps on the exact curve corresponds to a level crossing, where the quantum number for the z-component of spin shifts by one unit; the plot also shows an adiabatic-time evolution, which will be discussed later. In this work, we show how to obtain these quantum phase transition points (critical B_z values) on a quantum computer.

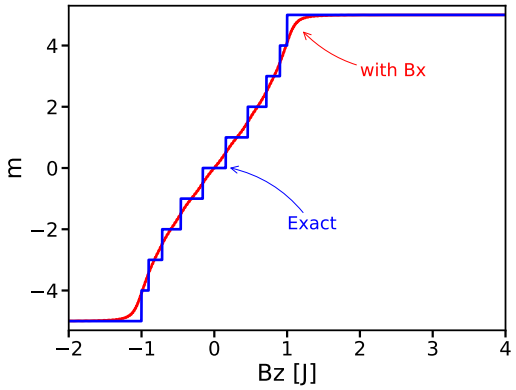

Figure 1. Magnetization versus the B_z field for a 10-site system. The blue curve labeled exact shows the magnetization for the ground state without any B_x field. The red curve shows the magnetization of a local adiabatic-evolved state from an all-up state with a local ramp of $\gamma = 50$ and 1000 Trotter steps (see Equation (4)). Here, we have set $B_x = 0.05J$.

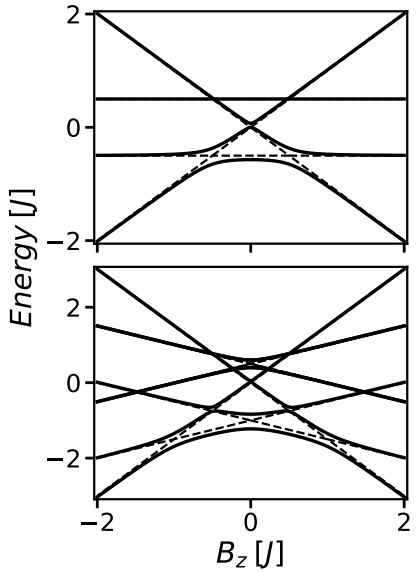

Figure 2. Energy diagram for a two-site (top panel) and three-site (bottom panel) system. The dotted lines are for the ideal system with $B_x = 0$; these curves have level crossings. The solid lines are the energies with $B_x = 0.2J$, which leads to avoided crossings everywhere for the ground state.

In adiabatic-state preparation, we start from the ground state of a Hamiltonian, which is easy to prepare, and then we slowly evolve the state using time evolution with a Hamiltonian that interpolates from the initial Hamiltonian to the target Hamiltonian. The amount of

diabatic excitations are determined by how fast the Hamiltonian changes near the avoided-crossing spectral gaps between the ground and excited states. The initial Hamiltonian can be thought of as a Hamiltonian with $J = 0$, or equivalently with $B_z \gg J$. Then, the magnetic field is ramped down to a final value (e.g., zero) where ideally we end up in the ground state of the final Hamiltonian. However, this cannot occur if there is additional symmetry in the Hamiltonian. Here, because $S^z = \sum_i \sigma_i^z/2$ commutes with H, we can simultaneously diagonalize both operators and this means the quantum number corresponding to the total z-component of spin (m) are unchanged during time evolution. Thus, we only stay in the ground state of a system with definite z-component of spin. This can be seen in Figure 2, where the dotted lines show a level crossing for a two- and three-site system.

In order to achieve adiabatic-state preparation, we must break the symmetry. We do so by adding a small B_x field, upon which $[S_z, H] \neq 0$. This means states that used to have different m quantum numbers are now coupled together. This can be seen in Figure 2, where the solid lines show avoided level crossings for a two- and three-site system with a B_x field. This then allows adiabatic-state preparation to take place, and if we go slow enough, we will have limited diabatic excitation out of the ground state. Figure 1 shows that with a B_x field one can traverse through all the magnetization sectors in a 10-site system. However, the B_x term changes the Hamiltonian and its energy levels. We only have quantum phase transitions when $B_x = 0$, which implies we must extrapolate to the $B_x \to 0$ limit. With the B_x term, the modified Hamiltonian is

$$H = -\sum_{i=1}^{L}\left[\frac{J}{4}\left(\sigma_i^x\sigma_{i+1}^x + \sigma_i^y\sigma_{i+1}^y\right) + \frac{B_x}{2}\sigma_i^x + \frac{B_z}{2}\sigma_i^z\right]. \tag{3}$$

The time evolution is implemented with a local adiabatic ramp [17,18], which is constructed to yield the same diabatic excitation for each time step of the time evolution. It does so by ramping faster when the gap to the first excited state is large and more slowly when the gap is small. It is determined by adjusting the rate $\frac{dB_z}{dt}$ according to the instantaneous energy gap $\Delta(B_z)$ such that $|\frac{dB_z}{dt}| \ll \Delta^2(B_z)$ [18]. This provides the highest fidelity ramp for a given total time of evolution.

The total time for the local ramp is determined by an adiabaticity parameter (γ). We require $\gamma \gg 1$ for an adiabatic ramp, where $\gamma = \frac{\Delta^2(B_z)}{|dB_z(t)/dt|}$. Starting from a magnetic field $B_{z,\text{initial}}$ and ramping down to a magnetic field $B_{z,\text{final}}$ the ramp time t is given by

$$t = -\gamma \int_{B_{z,\text{initial}}}^{B_{z,\text{final}}} \frac{dB_z}{\Delta^2(B_z)}. \tag{4}$$

where Δ is the energy difference between first excited state and ground state and the minus sign indicates that we are ramping down. One can either choose the adiabaticity parameter first, and determine the total time, or one can fix the total time and infer the adiabaticity parameter. A resulting local adiabatic ramp for a two- and three-site system is shown in Figure 3. The ramp was implemented via a Trotter product formula. We selected the adiabaticity parameter and the number of Trotter steps such that we can accurately determine the different steps in the magnetization; the magnetization then signals the different regions of the ground-state-phase diagram. Specifically, we fixed γ and increased the number of steps from a small number of total steps such that the magnetization switches to the next sector for all the B_x values. The goal is to implement the ramp with a small total number of steps so that depth of the circuits implemented on the quantum computer is reduced.

The same strategy is used on a quantum computer. We use the first-order Trotter product formula for the time-evolution operator from t_0 to t:

$$\mathbf{U}(t, t_0) \approx e^{-i\mathbf{H}(t-dt)dt} e^{-i\mathbf{H}(t-2dt)dt} \ldots e^{-i\mathbf{H}(t_0)dt}. \tag{5}$$

Then, each Trotter step further is decomposed into two qubit and single qubit gates so that it can be implemented on the IBM machines using their native gate set.

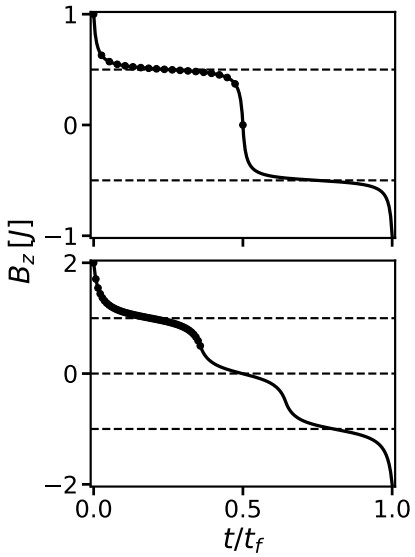

Figure 3. Local adiabatic ramp for a two-site (top panel) and three-site (bottom panel) system. For the two-site system, the solid line shows a ramp with 200 time steps and the solid circles are for 20 time steps. Here, we have set $B_x = 0.02J$ and $\gamma = 1.5$ for two sites. For the three-site system, we have taken $B_x = 0.08J$ and $\gamma = 2$ and the curves are similar (solid line, 200 time steps; solid circles, 50 time steps). The horizontal axis is the fractional time t/t_f for the 200 step ramp. We use an Akima spline interpolator to obtain the ramp in uniform time steps from uniform magnetic field steps used in evaluating the integral. One can see that the ramp goes slower near the crossing regions.

This procedure yields values for dt that are larger than is typical for Trotter decomposition; for example, for the two-site system we obtain $dt = 8.45/J$ for $B_x = 0.02J$ (see Figure 4). However, while the absolute value of dt is large, it is ameliorated by two factors. First, the non-commuting part of the Hamiltonian is entirely proportional to B_x, which is small, so that the effective small parameter is really dtB_x. Second, the leading-order commutator arising from the Baker–Campbell–Hausdorff (BCH) expansion of the time evolution from t_1 to t_2 when $\frac{dt}{2} < 1$ is further suppressed by the slowly varying magnetic field $B_z(t)$ as

$$\left| \frac{[H(t_1)dt, H(t_2)dt]}{2} \right| = \left| \frac{dt^2 B_x}{4} [B_z(t_2) - B_z(t_1)] \sum_{i=1}^{N} \sigma_i^y \right| \tag{6}$$

Thus, as long dB/dt is not too large, the error arising from Trotterization is manageable—this is expected because when the Hamiltonian is time independent, it commutes with itself at all times and no error arises from the BCH expansion. One additional source of Trotter error arises from the gate decomposition of the time evolution operator—here, the leading error is similarly proportional to $B_x(\frac{dt}{2})^2$. This is the leading order in BCH expansion when $\frac{dt}{2} < 1$, e.g., in our three-site experiments (see Figure 5). For two sites and three sites, we have confirmed empirically that the magnetization goes to the next sector with the given dt (run on a simulator). The behavior of the crossing points for a 1000 Trotter step evolution is shown in Figures 6 and 7. For larger systems, one might need to increase the number of Trotter steps so that dt is small and follows the adiabatic evolution more closely.

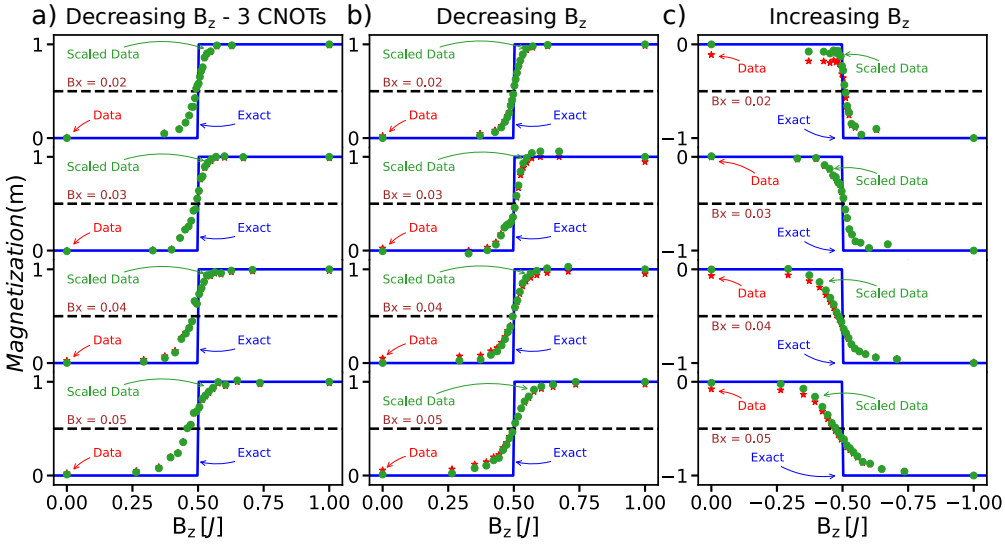

Figure 4. Magnetization versus B_z data for a two-site system. We use a local adiabatic ramp of 20 time steps with $\gamma = 1.5$, starting from the all-up state (**a**,**b**) and all-down state (**c**). Exact denotes the magnetization curve with $B_x = 0$. Data (red stars) denotes the values obtained from *ibmq_santiago* after measurement error mitigation [19]. The scaled data (green solid circles) are the experimental data after matching the known end points (see text). The leftmost panel uses the optimal two-qubit circuit with three CNOTs for the positive magnetization sector. The middle and rightmost panel uses the Trotterized circuit for the positive and negative magnetization sector respectively. The ramp with 20 steps turns to have $dt = 8.45/J$ for $B_x = 0.02J$, $dt = 5.3/J$ for $B_x = 0.03$, $dt = 4.07/J$ for $B_x = 0.04J$, $dt = 3.20/J$ for $B_x = 0.05J$ (see text for discussion). We use first-order Trotterization, as shown in Figure A4.

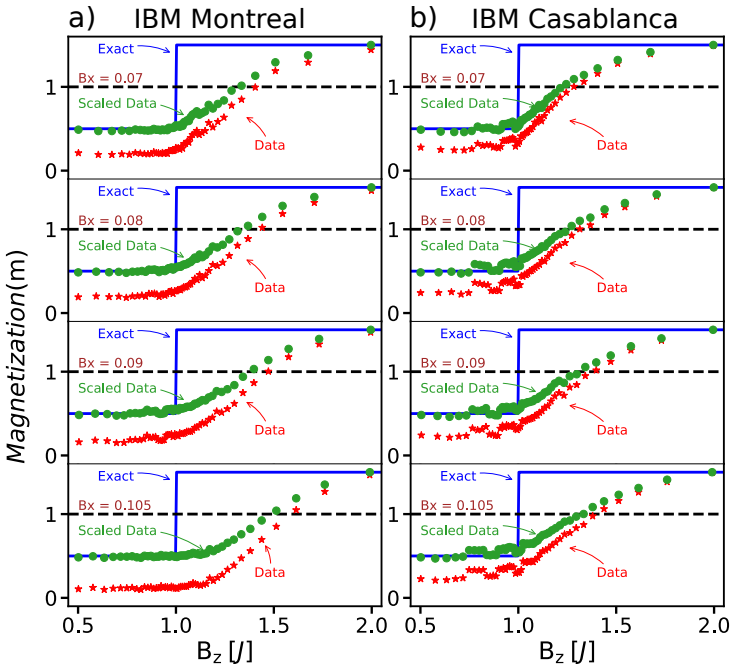

Figure 5. Experimental data after measurement-error mitigation (red stars) for the magnetization (positive) versus B_z on a three-site system with a local ramp starting from the ground state of all spins up on different backends; (**a**) and *ibmq_montreal* (**b**) *ibmq_casablanca*. Further scaled data (both backends) are shown as green solid circles. We used 50 time steps and $\gamma = 2$ for the ramp. The ramp with 50 steps turns to have $dt = 0.94/J$ for $B_x = 0.07J$, $dt = 0.80/J$ for $B_x = 0.08J$, $dt = 0.70/J$ for $B_x = 0.09J$, $dt = 0.58/J$ for $B_x = 0.105$ (see text for discussion). We used first-order Trotterization, as shown in Figure A5.

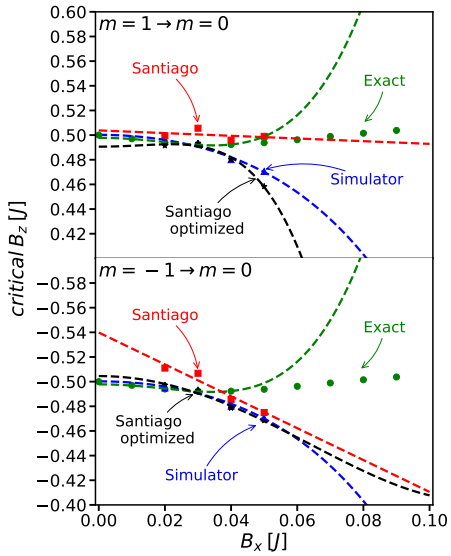

Figure 6. Estimation of the quantum phase transition for a two-site model using extrapolation to the $B_x \rightarrow 0$ limit. To obtain the critical value for each B_x, we interpolate the data points (scaled) and determine where the magnetization is equal to 0.5. For the exact simulation (green solid circles), we have used local adiabatic ramp with 1000 time steps and γ value 1.5. The simulator (blue triangles) and quantum computer (red solid squares for circuit without optimization and black stars for circuit with optimization) use 20 time steps. The exact value at $B_x = 0.0$ is shown explicitly (green solid circles) to indicate where the actual phase transition is. The initial state has all up spins for the top panel and all down spins for the bottom panel. The green dotted line shows the quartic fit of the exact results to the first four data points. The blue dotted line is the quartic fit to the simulator values. The red dotted line is the linear fit for the quantum computer calculation with no circuit optimization. Black dotted line is the quartic fit for optimized circuit data with three CNOTs.

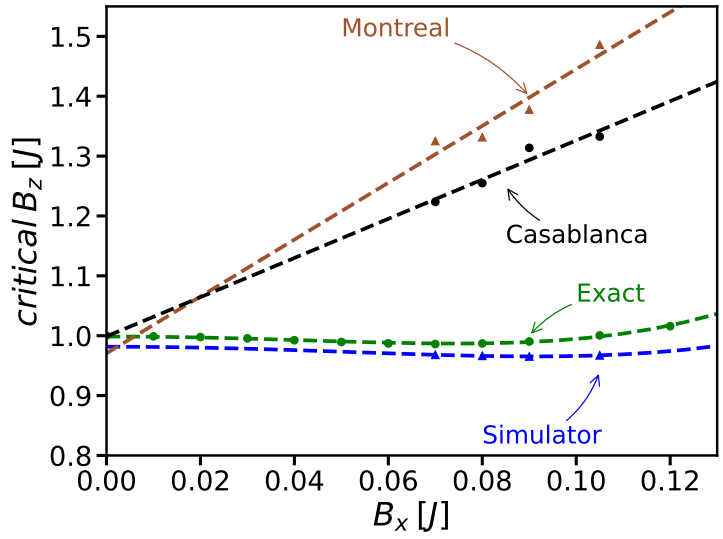

Figure 7. Estimation of the quantum phase transition for three sites using extrapolation to the $B_x \rightarrow 0$ limit. This case is for an initial state with all spins up. To obtain the critical value for each B_x, we use an interpolation of the scaled data points. Brown triangles correspond to data from *ibmq_montreal* and black solid circles for *ibmq_casablanca*. The corresponding colored dotted lines show the linear fit for these data points. For exact calculation (green solid circles), we use 1000 time steps and $\gamma = 2$. For the simulator (blue triangles) and the quantum computer, we use 50 steps. The exact value at $B_x = 0.0$ is shown explicitly (green solid circles) to indicate where the phase transition is actually located. The quartic fit to the exact and simulator data points are shown with the green and blue dotted lines respectively.

The determination of the phase diagram then proceeds as follows: (i) we initialize the system in a state that is all up and with the magnetic field equal to $B_{z\ \mathrm{initial}}$ and with a fixed value for B_x; (ii) we evolve the system from t_0 to t using the local adiabatic ramp for $B_z(t)$; (iii) at each time step, we measure the magnetization; (iv) using the magnetization, we determine the critical value of B_z, which corresponds to the midpoint of the step in the magnetization between two successive m quantum numbers; (v) we repeat these steps for a different value of B_x; and (vi) we extrapolate the critical B_z field to the limit where $B_x \to 0$.

Extrapolation to find critical B_z can be done by fitting polynomial curves to the data. The σ^x operator only connects states with definite m eigenvalues that are shifted by one: $n = m \pm 1$, for $\langle n| \sum_i \sigma_i^x |m\rangle \neq 0$. Then, a simple argument using perturbation theory shows that the perturbed energy eigenvalues are functions of even powers of B_x for small B_x values. This means that when we try to extrapolate the exact results for the critical B_z field, we should use a dependence on even powers of B_x only. Hence, we include only quadratic and quartic terms in the fitting curve for the data generated on a classical computer via exact diagonalization.

For the data from a quantum computer, we instead fit with a linear regression, because the noise on the quantum computer changes the behavior from even powers of B_x to a nearly linear dependence. When quantum computers become capable of doing longer time runs, with less noise and decoherence, then, we can fit a quadratic polynomial without the linear term for smaller B_x values to estimate the critical point in a more systematic way.

3. Results

In order to demonstrate the technique, we first examine a two-site system. At large B_z, the ground state has all spins aligned in the up direction; the calculation starts with this state. The system is time evolved using the Trotter product formula using a local adiabatic ramp given in Equation (4). The integral produces $t(B_z)$ with uniform steps in B_z. We convert to $B_z(t)$ with uniform steps in t by inverting the map and employing an Akima spline, which preserves the shape (see Figure 3). We choose γ and the number of time steps such that the time evolution spans the change in magnetization by one full unit (see Figure 4). We repeat the same procedure to find the time evolution for each B_x value. The time evolution is implemented in the quantum simulation using two-qubit and single-qubit gates. We decompose each Trotter step into the XY part, the B_x part, and the B_z part:

$$\mathbf{U}_{12}(t+dt,t) = \exp\left[i[\frac{J}{4}\left(\sigma_1^x\sigma_2^x + \sigma_1^y\sigma_2^y\right) + \frac{1}{2}B_x(\sigma_1^x+\sigma_2^x) + \frac{1}{2}B_z(t)(\sigma_1^z+\sigma_2^z)]dt\right] \quad (7)$$

$$\approx \exp\left[i\frac{B_z(t)}{2}(\sigma_1^z+\sigma_2^z)dt\right]\exp\left[i\frac{B_x}{2}(\sigma_1^x+\sigma_2^x)dt\right]\exp\left[i\frac{J}{4}\left(\sigma_1^x\sigma_2^x+\sigma_1^y\sigma_2^y\right)dt\right] \quad (8)$$

The XY part is further decomposed to implement in the quantum simulation using two CNOTs [20], as shown in Figure 8. The B_x part and B_z part are implemented using single-qubit gates.

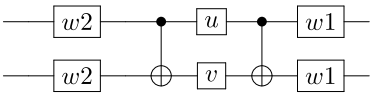

Figure 8. Quantum circuit for the evaluation of $\exp\left(-i\mathcal{H}_{12}^{XY}dt\right)$. This is the time evolution circuit for the XY part in each Trotter step for the two-site system. $w_1 = \frac{\mathbf{1}-i\sigma^x}{\sqrt{2}}$, $w_2 = w_1^+$, $u = \exp\left(i\frac{J}{4}\sigma^x dt\right)$, $v = \exp\left(i\frac{J}{4}\sigma^z dt\right)$.

For the two-site case, we decrease B_z from $B_z = 1.0J$ to $B_z = 0.0J$ to go through the first transition point (we have set $J = 1$ in all our calculations). We use B_x values given by $0.02J$, $0.03J$, $0.04J$, and $0.05J$ (see Figure 4). For the exact curve we use 1000 Trotter steps, but since we cannot achieve high fidelity in currently available quantum computers for such a large number of Trotter steps, we look for a similar trend in the crossing point so that a fewer number of Trotter time steps is sufficient (see Figure 6). For a two-site

system the time evolution could be implemented with three CNOTs [20] to achieve high fidelity. But since these short-depth circuits are not available in general for a large system size, we consider the explicit implementation of a Trotter circuit to enable a comparison with larger system size. Later, we also show results from a three-CNOTs version of the circuit. With 20 Trotter steps the simulator data showed reasonable results. We use an Akima spline to fit the magnetization versus B_z data to have a smooth curve, allowing us to determine the transition point. From the simulator data we find the crossing points where the magnetization is equal to 0.5. A quartic fit was performed to the crossing points from the simulator data and we obtained a critical value of $B_z = 0.500J$. This result is reasonable, since performing a quartic fit to the first four data points in the exact curve yields an extrapolated value equal to $0.498J$.

We perform the quantum computer run on the *ibmq_santiago*. The data obtained from the quantum computer with measurement-error mitigation [19] is shown in Figure 4. As a secondary error mitigation technique, we scale the data so that the initial and final magnetization values of the quantum computer data match that of the quantum simulator. This stretches and shifts the data so that the end points have the correct values (see Figure 4). Such scaling is common to correct from decoherence and noise, and it improves the data analysis [21–24]. Here, scaling is based on the fact that for small B_x values the magnetization approximately follows steps as a function of B_z. At our initial B_z, the magnetization corresponds to all spins aligned up; our final magnetization decreases by a single unit for each transition. When simulator values are difficult to obtain (e.g., for a large N) the final B_z can be taken where the curve goes flat. The experiment is repeated for different B_x values and the corresponding crossing points are plotted in the Figure 6. Since the data obtained was noisy we fitted a linear extrapolation curve to capture the trend in the quantum computer data. The extrapolated critical B_z value is $0.504J$, which is close to the actual value of transition, which occurs at $0.5J$.

For the second case, we examine the transition from $m = -1$ to $m = 0$. While, formally, this should be the same as the case for $m = 1$ to $m = 0$, because the $|1\rangle$ state of a quantum computer is the excited state, decoherence effects should be larger for this case. Here, the initial state has both spins down. The procedure is similar to what we explained above. A quartic fit to the simulator values obtained a critical value of $-0.50J$. A quartic fit to the first four data points of the exact crossings (for γ = 1.5 and 1000 Trotter steps), obtained an extrapolated value of $-0.498J$. The data obtained from the IBM quantum computer is shown in Figure 4. The crossing points were found from the scaled data for each B_x value. A linear fit to the quantum computer data gave the critical value to be $-0.54J$.

For the two-site model, we also performed the experiment in an *ibmq_santiago* machine after optimizing the circuits with a level-three optimization in the IBM Qiskit transpiler. This reduced the number of CNOT gates to three for each time step. This is because any two-qubit unitary operation can be represented using three-CNOT gates [20,25]. The read-out-corrected data are shown in Figure 4. The crossing points from these fixed-depth circuits are shown in Figure 6. These values are closer to the simulator values than the Trotter data, as expected. A quartic fit to these data obtained a critical B_z value of $0.491J$ starting from all spins aligned up, and $-0.504J$ starting from all spins aligned down. This kind of an efficient fixed-depth decomposition is not known in general for more than two qubits. But for certain models, efficient fixed-depth circuit decompositions can be found [26]. These type of fixed-depth circuits can improve the performance of our method by reducing the number of gates in an adiabatic-time evolution as Trotter decomposition becomes increasingly costly with larger system sizes and more time evolution steps [27].

Now, we move on to the three-site periodic system. We start with all spins up. The time evolution circuit for the XY part is implemented pairwise using the XY part of the two-qubit circuit for each Trotter step. The data obtained from the quantum computer with measurement-error mitigation is shown in Figure 5, along with the scaled data which matches the end points from the simulator data. The extrapolations are shown in Figure 7. A quartic fit to the exact values gives the critical B_z value to be $0.999J$. A quartic fit to the

simulator values gives the critical B_z to be $0.982J$. The linear fit to the crossings from the scaled data of the IBM quantum computer give the phase transition point to be $0.971J$ for *ibmq_montreal* and $0.999J$ for the *ibmq_casablanca*. The actual transition is at $1.0J$. These fitted values are reasonably close to the actual value.

4. Discussion

In this work, we propose a method for finding zero-temperature phase diagrams that are robust and can be carried out on quantum computers. The approach requires us to introduce a symmetry-breaking term into the Hamiltonian, determine approximate phase diagrams for the symmetry-broken system, and then extrapolate to the limit where the symmetry-breaking field vanishes. To verify that this approach works, we have worked out practical details for how to run these circuits on a quantum computer when the number of spins is two or three. The results from the quantum computers agree well with the exact results and are able to predict the phase boundaries within a few percent. This illustrates that the approach used here, based on adiabatic-state preparation, can work on NISQ machines and has the potential to be able to be applied to larger systems, even ones where we do not know the phase diagram *a priori*.

Note that the case we examined here, the XY model in a z-oriented magnetic field, is probably the most difficult problem to examine, because the number of level crossings increases with the system size. For most quantum phase transitions between different symmetry states, the number of phase boundaries should depend only weakly on the system size.

In order to show that this approach also applies to larger systems, we simulate the magnetization for a 10-site system in Figure 1 using a similar local adiabatic-time evolution for 1000 Trotter steps for $\gamma = 50$. Extracting the phase transitions using our methodology works well for such a system, as can be seen by comparing the two lines in the figure.

As the system size increases, finer time-evolution steps are required to prepare the state due to the higher density of energy eigenstates. This would require the quantum hardware to have better gate fidelity and less measurement errors so that the overall error in magnetization remains low. Nevertheless, for larger and more complex systems, using quantum computers is a potential way to handle quantum-simulation-related problems, as classical computers cannot deal with very large Hilbert spaces in general [3,5]. Once better quantum hardware is available, our method could be applied to finding the critical points for larger quantum systems.

Author Contributions: Conceptualization, J.K.F.; methodology, J.K.F., E.Z., Z.Z. and A.F.; software, A.F., E.Z. and Z.Z.; validation, J.F.K. and A.F.K.; formal analysis, A.F.; data curation, A.F.; writing—original draft preparation, all authors; writing—review and editing, all authors; visualization, A.F.; supervision, J.K.F. and A.F.K.; project administration, J.K.F.; funding acquisition, J.K.F. and A.F.K. All authors have read and agreed to the published version of the manuscript.

Funding: For this work, the planning, formal development, and circuit development (A.F., J.K.F. and A.F.K.), as well as part of the manuscript writing (J.K.F. and A.F.K.) was supported by the Department of Energy, Office of Basic Energy Sciences, Division of Materials Sciences and Engineering under Grant No. DE-SC0019469. The circuit execution and manuscript writing (A.F.) was supported by the National Science Foundation under Grant No. NSF DMR-1752713. E.Z. was supported by the U.S. Department of Energy, Office of Science, Office of Advanced Scientific Computing Research (ASCR), Quantum Computing Application Teams (QCATS) Program, under field work proposal number ERKJ347 for her work in the summer of 2020 in developing the formalism and exact diagonalization codes for this project. J.K.F. was also supported by the McDevitt bequest at Georgetown.

Data Availability Statement: The data for the figures are available at https://doi.org/10.5061/dryad.z8w9ghxdq (accessed on 27 Januray 2022).

Acknowledgments: We acknowledge fruitful discussions with Brian Rost. We acknowledge the use of IBMQ via the IBM Q Hub at NC State for this work. The views expressed are those of the authors

and do not reflect the official policy or position of the IBM Q Hub at NC State, IBM, or the IBM Q team. We acknowledge the use of the Qiskit software package [28] for doing the quantum simulations.

Conflicts of Interest: The authors declare no conflict of interest.

Appendix A. Experimental Details

The two-site experiments were performed on *ibmq_santiago* (see Figure A1) and the three-site experiments were performed on *ibmq_montreal* and *ibmq_casablanca* (see Figures A2 and A3). The two-site experiments without circuit optimization were done on 18 July 2021 (for Figure 4b,c). Three-CNOTs version of two qubits for positive magnetization were run on 7 September 2021 (for Figure 4). Three-CNOTs version of two-site experiments for negative magnetization were run on 7 September 2021 and 14 September 2021. The three-qubit experiments on *ibmq_montreal* were performed on 7 and 12 July 2021 (for Figure 5a). The three-qubit experiments on *ibmq_casablanca* were performed on 12 July 2021 (for Figure 5b). The calibration data during the days in which the experiment were performed along with qasm codes of experiments are given in the supplemental data at https://doi.org/10.5061/dryad.z8w9ghxdq (accessed on 27 Jan 2022). Relevant calibration data for the qubits used are also given in the following Tables A1–A6. We chose these qubits because the corresponding two-qubit CNOT errors were lower than for other qubits in the layout. Other calibration details of the cloud-based quantum computers are available, but the overwhelming effect on the results originates in the two-qubit CNOT errors, as single-qubit errors are usually lower than the CNOT errors. The data shown in the main figures are after measurement-error mitigation using the builtin routines in QISKIT [19,28]. We further scaled the data to match the end point values to that of quantum simulator, as mentioned in the main text (see Figures 4 and 5). The circuit diagrams for the two-site and three-site experiments are shown in Figures A4 and A5, respectively.

Table A1. Calibration data for *ibmq_santiago* on 18 July 2021.

Qubits	T1 (μs)	T2 (μs)	Readout Error	CNOT Connection	CNOT Error
3	221.6	86.0	0.006	3-4 3-2	0.0049 0.0061
4	100.0	137.0	0.013	4-3	0.0049

Table A2. Calibration data for *ibmq_santiago* on 7 September 2021.

Qubits	T1 (μs)	T2 (μs)	Readout Error	CNOT Connection	CNOT Error
3	65.2	64.3	0.012	3-4 3-2	0.0071 0.0068
4	101.1	158.0	0.019	4-3	0.0071

Table A3. Calibration data for *ibmq_santiago* on 14 September 2021.

Qubits	T1 (μs)	T2 (μs)	Readout Error	CNOT Connection	CNOT Error
3	103.1	866.0	0.007	3-4 3-2	0.0057 0.0067
4	115.0	171.0	0.013	4-3	0.0057

Table A4. Calibration data for *ibmq_casablanca* on 12 July 2021.

Qubits	T1 (µs)	T2 (µs)	Readout Error	CNOT Connection	CNOT Error
3	80.9	93.4	0.016	3-5 3-1	0.0088 0.0094
4	100.2	59.3	0.022	4-5	0.0083
5	66.5	134.2	0.010	5-6 5-4 5-3	0.0083 0.0083 0.0088
6	85.4	187.2	0.015	6-5	0.0083

Table A5. Calibration data for *ibmq_montreal* on 7 July 2021.

Qubits	T1 (µs)	T2 (µs)	Readout Error	CNOT Connection	CNOT Error
0	129.1	46.5	0.012	0-1	0.0063
1	127.2	20.3	0.015	1-4 1-2 1-0	0.0082 0.0113 0.0063
2	71.0	77.1	0.025	3-2 2-1	0.0220 0.0113
4	106.5	156.4	0.013	4-7 4-1	0.0071 0.0082

Table A6. Calibration data for *ibmq_montreal* on 12 July 2021.

Qubits	T1 (µs)	T2 (µs)	Readout Error	CNOT Connection	CNOT Error
0	121.7	68.0	0.016	0-1	0.0066
1	127.2	20.3	0.019	1-4 1-2 1-0	0.0079 0.0112 0.0066
2	89.2	45.3	0.021	2-3 2-1	0.0216 0.0112
4	105.2	103.7	0.012	4-7 4-1	0.0107 0.0079

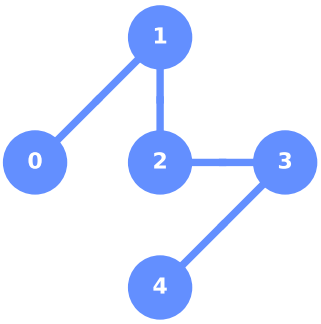

Figure A1. *ibmq_santiago* layout. For the two-site experiment shown in Figure 4, qubits 3 and 4 were used as system qubits.

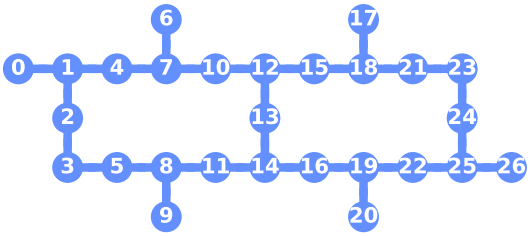

Figure A2. *ibmq_montreal* layout. For the three-site experiment shown in Figure 5, qubits 0,2,4 were used as system qubits in the QISKIT simulation.

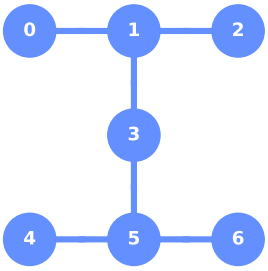

Figure A3. *ibmq_casablanca* layout. For the three-site experiment shown in Figure 5, qubits 3,4,6 were used as system qubits in the QISKIT simulation.

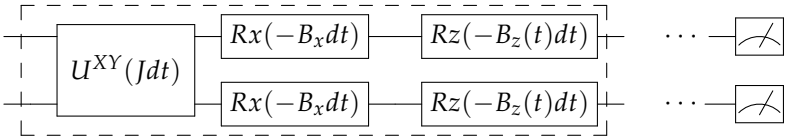

Figure A4. Quantum circuit for the evaluation of magnetization of the two-site system. The time evolution is performed using Trotterization. The gates boxed with dashed lines show the time-evolution circuit for each Trotter step, as given in Equation (7). This block is repeated with appropriate $B_z(t)$ coefficient to get total time evolution. The $U^{XY}(Jdt) = \exp\left[i\frac{J}{4}\left(\sigma_1^x\sigma_2^x + \sigma_1^y\sigma_2^y\right)dt\right]$ is the time evolution of XY part given in Figure 8. The $Rx(\theta) = \exp\left(-i\frac{\theta}{2}\sigma^x\right)$ and $Rz(\theta) = \exp\left(-i\frac{\theta}{2}\sigma^z\right)$.

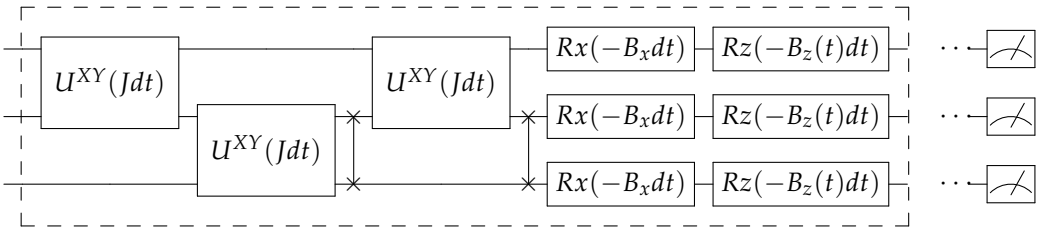

Figure A5. Quantum circuit for the evaluation of magnetization of the three-site system. The time evolution is performed using Trotterization. The gates boxed with dashed lines show the time-evolution circuit for each Trotter step. This block is repeated with appropriate $B_z(t)$ coefficient to get total evolution, as described in Equation (5). The $U^{XY}(Jdt)$ is the time evolution of XY part given in Figure 8. The $Rx(\theta) = \exp\left(-i\frac{\theta}{2}\sigma^x\right)$ and $Rz(\theta) = \exp\left(-i\frac{\theta}{2}\sigma^z\right)$. The swap gates are used to show the appropriate connection of qubits for the periodic term.

References

1. Lloyd, S. Universal quantum simulators. *Science* **1996**, *273*, 1073–1078. [CrossRef] [PubMed]
2. Abrams, D.S.; Lloyd, S. Simulation of many-body Fermi systems on a universal quantum computer. *Phys. Rev. Lett.* **1997**, *79*, 2586. [CrossRef]
3. Georgescu, I.M.; Ashhab, S.; Nori, F. Quantum simulation. *Rev. Mod. Phys.* **2014**, *86*, 153. [CrossRef]
4. Montanaro, A. Quantum algorithms: An overview. *NPJ Quantum Inf.* **2016**, *2*, 1–8. [CrossRef]
5. Childs, A.M.; Maslov, D.; Nam, Y.; Ross, N.J.; Su, Y. Toward the first quantum simulation with quantum speedup. *Proc. Natl. Acad. Sci. USA* **2018**, *115*, 9456–9461. [CrossRef]

6. Qin, M.; Schäfer, T.; Andergassen, S.; Corboz, P.; Gull, E. The Hubbard model: A computational perspective. *arXiv* **2021**, arXiv:2104.00064.
7. Vojta, M. Quantum phase transitions. *Rep. Prog. Phys.* **2003**, *66*, 2069. [CrossRef]
8. Hubbard, J. Electron correlations in narrow energy bands. *Proc. R. Soc. Lond. Ser. Math. Phys. Sci.* **1963**, *276*, 238–257.
9. Farhi, E.; Goldstone, J.; Gutmann, S. A quantum approximate optimization algorithm. *arXiv* **2014**, arXiv:1411.4028.
10. Chen, X.; Ruschhaupt, A.; Schmidt, S.; del Campo, A.; Guéry-Odelin, D.; Muga, J.G. Fast optimal frictionless atom cooling in harmonic traps: Shortcut to adiabaticity. *Phys. Rev. Lett.* **2010**, *104*, 063002. [CrossRef]
11. Guéry-Odelin, D.; Ruschhaupt, A.; Kiely, A.; Torrontegui, E.; Martínez-Garaot, S.; Muga, J.G. Shortcuts to adiabaticity: Concepts, methods, and applications. *Rev. Mod. Phys.* **2019**, *91*, 045001. [CrossRef]
12. Bak, P.; Bruinsma, R. One-Dimensional Ising Model and the Complete Devil's Staircase. *Phys. Rev. Lett.* **1982**, *49*, 249–251. [CrossRef]
13. Richerme, P.; Senko, C.; Korenblit, S.; Smith, J.; Lee, A.; Islam, R.; Campbell, W.C.; Monroe, C. Quantum catalysis of magnetic phase transitions in a quantum simulator. *Phys. Rev. Lett.* **2013**, *111*, 100506. [CrossRef] [PubMed]
14. Jordan, P.; Wigner, E. Pauli's equivalence prohibition. *Z. Phys.* **1928**, *47*, 631. [CrossRef]
15. Lieb, E.; Schultz, T.; Mattis, D. Two soluble models of an antiferromagnetic chain. *Ann. Phys.* **1961**, *16*, 407–466. [CrossRef]
16. Mbeng, G.B.; Russomanno, A.; Santoro, G.E. The quantum Ising chain for beginners. *arXiv* **2020**, arXiv:2009.09208.
17. Roland, J.; Cerf, N.J. Quantum search by local adiabatic evolution. *Phys. Rev. A* **2002**, *65*, 042308. [CrossRef]
18. Richerme, P.; Senko, C.; Smith, J.; Lee, A.; Korenblit, S.; Monroe, C. Experimental performance of a quantum simulator: Optimizing adiabatic evolution and identifying many-body ground states. *Phys. Rev. A* **2013**, *88*, 012334. [CrossRef]
19. Andersson, S.; Asfaw, A.; Corcoles, A.; Bello, L.; Ben-Haim, Y.; Bozzo-Rey, M.; Bravyi, S.; Bronn, N.; Capelluto, L.; Vazquez, A.C.; et al. Learn Quantum Computation Using Qiskit. Available online: http://community.qiskit.org/textbook (accessed on 24 January 2022).
20. Vidal, G.; Dawson, C.M. A universal quantum circuit for two-qubit transformations with three CNOT gates. *Phys. Rev. A* **2004**, *69*, 010301. [CrossRef]
21. Chiesa, A.; Tacchino, F.; Grossi, M.; Santini, P.; Tavernelli, I.; Gerace, D.; Carretta, S. Quantum hardware simulating four-dimensional inelastic neutron scattering. *Nat. Phys.* **2019**, *15*, 455–459. [CrossRef]
22. Francis, A.; Freericks, J.; Kemper, A. Quantum computation of magnon spectra. *Phys. Rev. B* **2020**, *101*, 014411. [CrossRef]
23. Rost, B.; Del Re, L.; Earnest, N.; Kemper, A.F.; Jones, B.; Freericks, J.K. Demonstrating robust simulation of driven-dissipative problems on near-term quantum computers. *arXiv* **2021**, arXiv:2108.01183.
24. Arute, F.; Arya, K.; Babbush, R.; Bacon, D.; Bardin, J.C.; Barends, R.; Bengtsson, A.; Boixo, S.; Broughton, M.; Buckley, B.B.; et al. Observation of separated dynamics of charge and spin in the fermi-hubbard model. *arXiv* **2020**, arXiv:2010.07965.
25. Kraus, B.; Cirac, J.I. Optimal Creation of Entanglement Using a Two–Qubit Gate. *Phys. Rev. A* **2001**, *63*, 062309. [CrossRef]
26. Kökcü, E.; Steckmann, T.; Freericks, J.; Dumitrescu, E.F.; Kemper, A.F. Fixed depth hamiltonian simulation via cartan decomposition. *arXiv* **2021**, arXiv:2104.00728.
27. Childs, A.M.; Su, Y.; Tran, M.C.; Wiebe, N.; Zhu, S. Theory of trotter error with commutator scaling. *Phys. Rev. X* **2021**, *11*, 011020. [CrossRef]
28. Aleksandrowicz, G.; Alexander, T.; Barkoutsos, P.; Bello, L.; Ben-Haim, Y.; Bucher, D.; Cabrera-Hernández, F.J.; Carballo-Franquis, J.; Chen, A.; Chen, C.F.; et al. Qiskit: An Open-Source Framework for Quantum Computing. 2019. Available online: https://zenodo.org/record/2562111#.YlYzptNByUl (accessed on 21 February 2022).